Circulation and Modification of Warm Deep Water on the Central Amundsen Shelf

H. K. HA,* A. K. WÅHLIN,+ T. W. KIM,# S. H. LEE,# J. H. LEE,@ H. J. LEE,# C. S. HONG,@
L. ARNEBORG,+ G. BJÖRK,+ AND O. KALÉN+

*Korea Polar Research Institute, and Department of Oceanography, Inha University, Incheon, South Korea
+Department of Earth Sciences, University of Gothenburg, Gothenburg, Sweden
#Korea Polar Research Institute, Incheon, South Korea
@Korea Institute of Ocean Science and Technology, Ansan, South Korea

(Manuscript received 29 October 2013, in final form 23 December 2013)

ABSTRACT

The circulation pathways and subsurface cooling and freshening of warm deep water on the central Amundsen Sea shelf are deduced from hydrographic transects and four subsurface moorings. The Amundsen Sea continental shelf is intersected by the Dotson trough (DT), leading from the outer shelf to the deep basins on the inner shelf. During the measurement period, warm deep water was observed to flow southward on the eastern side of DT in approximate geostrophic balance. A northward outflow from the shelf was also observed along the bottom in the western side of DT. Estimates of the flow rate suggest that up to one-third of the inflowing warm deep water leaves the shelf area below the thermocline in this deep outflow. The deep current was 1.2°C colder and 0.3 psu fresher than the inflow, but still warm, salty, and dense compared to the overlying water mass. The temperature and salinity properties suggest that the cooling and freshening process is induced by subsurface melting of glacial ice, possibly from basal melting of Dotson and Getz ice shelves. New heat budgets are presented, with a southward oceanic heat transport of 3.3 TW on the eastern side of the DT, a northward oceanic heat transport of 0.5–1.6 TW on the western side, and an ocean-to-glacier heat flux of 0.9–2.53 TW, equivalent to melting glacial ice at the rate of 83–237 km^3 yr^{-1}. Recent satellite-based estimates of basal melt rates for the glaciers suggest comparable values for the Getz and Dotson ice shelves.

1. Introduction

The Amundsen Sea continental shelf is the terminus of the most rapidly melting parts of the West Antarctic Ice Sheet (Rignot et al. 2008; Pritchard et al. 2012). This is likely due to an increased oceanic heat supply from warm, salty ocean currents carrying circumpolar deep water (CDW) below the floating tongues of glacial ice in this region (Jenkins et al. 2010; Jacobs et al. 2011; Pritchard et al. 2012). The shelf area is separated into an eastern and a central part by a 300–400-m shallow ridge extending from the coast to the shelf break along 111°–116°W (Fig. 1). The focus here

is on the central part, where the Dotson trough (DT) leads from the shelf break to an irregularly shaped inner shelf basin with a maximum depth of 1400 m. The basin continues underneath the Getz ice shelf (GIS), the seventh largest ice shelf in Antarctica and the only terminus of the rapidly thinning Getz Glacier (Pritchard et al. 2009, 2012). Because of prevailing harsh weather and ice conditions, it is still undersampled with regard to the ocean circulation. A southward flow of warm CDW in DT has been observed along the bottom on the outer shelf, being banked up along the eastern flank in approximate geostrophic balance (Wåhlin et al. 2010, 2013; Arneborg et al. 2012). The flow is characterized by strong barotropic fluctuations induced by wind bursts (Wåhlin et al. 2013), and a net southward baroclinic flow of warm dense water in the bottom layer (Arneborg et al. 2012; Wåhlin et al. 2013) in similarity with the inflow farther east (Assmann et al. 2013). The circulation pathways of the deep flow on the central shelf are still unknown, as are the oceanic heat and freshwater budgets. Here we use new observations from shipborne transects

ⓐ Denotes Open Access content.

Corresponding author address: A. K. Wåhlin, Department of Earth Sciences, University of Gothenburg, PB 460, 405 30 Gothenburg, Sweden.
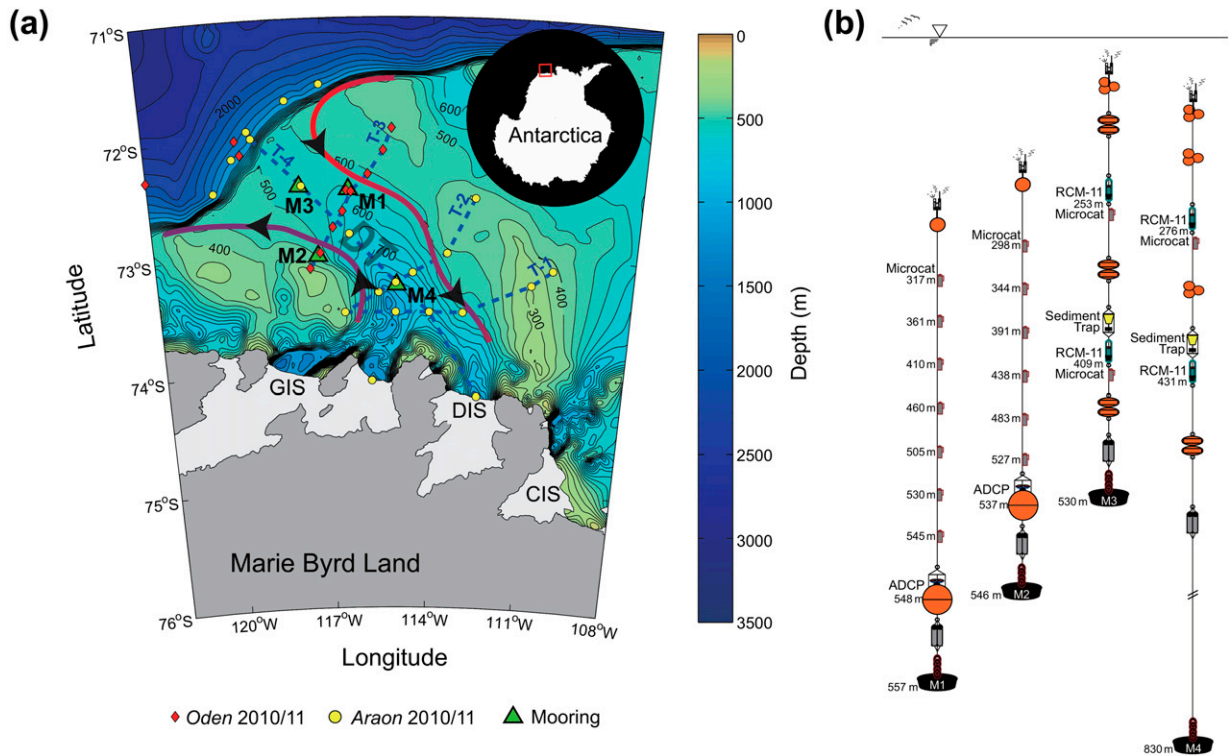E-mail: awahlin@gu.se

FIG. 1. (a) Map of the study area (rectangle in the inset) showing CTD/LADCP transects (yellow dots and red rhombs). Black lines are isobaths at 50-m intervals from 0 to 1000 m and 200-m intervals thereafter. Bathymetry is from Nitsche et al. (2007). Labels represent GIS, Dotson ice shelf (DIS), Crosson ice shelf (CIS), and DT. Mooring stations are indicated by green triangles at the following positions: M1 at 72° 27.41′S, 116° 20.76′W (557-m depth); M2 at 73° 00.99′S, 117° 14.94′W (546-m depth); M3 at 72° 24.16′S, 117° 43.34′W (530-m depth); and M4 at 73° 16.28′S, 114° 58.23′W (830-m depth). The red line with thick arrows indicates the proposed flow pathway from the current results. (b) Design sketches of the subsurface moorings.

and moored instruments to examine the circulation pattern and estimate the freshwater and heat budgets.

2. Methods

The data were collected during summer 2010/11 with the *Oden* (24–26 December 2010) and the *Araon* (3–6 January 2011). Vertical profiles of temperature, salinity, and currents were acquired with a CTD [SeaBird Electronics (SBE) 911+] and a 300-kHz lowered acoustic Doppler current profiler (LADCP) from Teledyne RD Instruments (RDI). The processing of the LADCP data was done according to Thurnherr (2010). The velocity profiles were detided using a 10-component barotropic tide model (Padman et al. 2002), and velocity shear was obtained using an inverse shear solution (Visbeck 2002). Geostrophic velocities normal to the CTD transects were calculated by vertical integration of the thermal wind relation, using 300 m as the reference depth.

Four bottom-mounted moorings measuring temperature, salinity, and velocity were also deployed in the trough (Fig. 1). Mooring M1 was placed on the eastern

side of the trough, M2 and M3 on the western side, and M4 in the center. M1 was deployed in February 2010 and recovered in March 2012, while M2, M3, and M4 were deployed in December 2010 and recovered in March 2012. M1 and M2 consisted of an array of six MicroCATs (SBE-37SMP) at 15–50-m intervals and a 150-kHz ADCP (RDI, QuarterMaster) that recorded vertical profiles of temperature, salinity, and velocity (Fig. 1b) from the bottom up to 320 m. M3 and M4 were equipped with two Doppler current meters (Aanderaa, RCM-11) and one or two MicroCATs (SBE-37SMP).

The oceanic heat flux through a cross-trough transect is given by

$$\text{HF}_{\text{IN}} = \rho C_P \int_{X_E}^{X_W} \int_{-D}^{-d} \overline{[T(z,t) - T_R]U_P} \, dz \, dx, \quad (1)$$

where ρ is density, C_P is heat capacity, $x = X_E$, X_W are the eastern and western lateral boundaries, $z = -D$ is the ocean bottom, $z = -d$ is the top of the mooring, $T(z,t)$ is the mooring temperature, T_R is the surface freezing temperature, and U_P is the velocity component parallel to
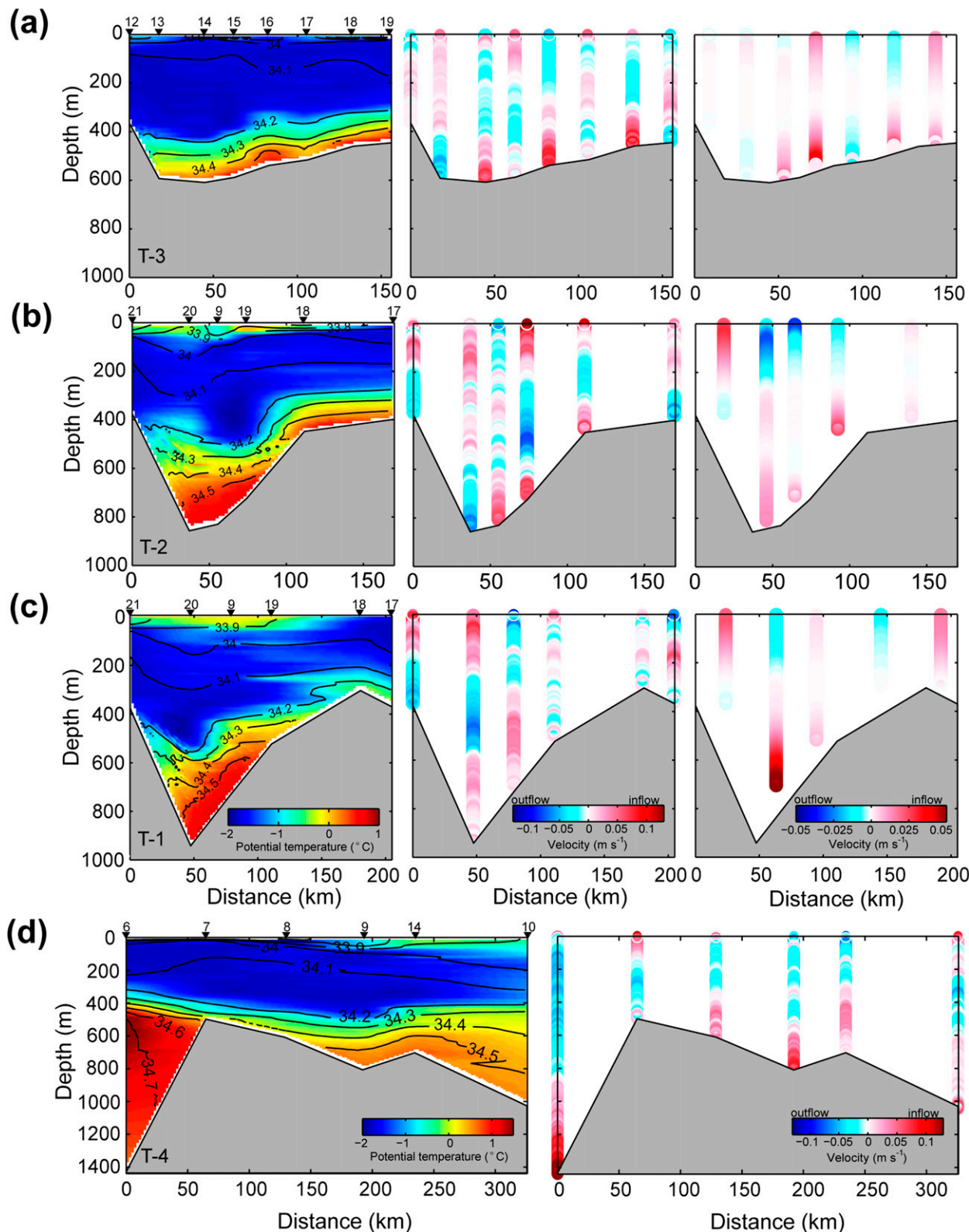
FIG. 2. Water column structure and water mass transport in the Dotson trough. (a)–(c) Cross-trough sections (T-3, T-2 and T-1) of (left) temperature with isohalines, (middle) LADCP shear velocity, and (right) geostrophic velocities. Positive velocity indicates inflow toward the ice shelf. For location of sections see Fig. 1. (d) Along-trough section (T-4) of (left) temperature with isohalines and (right) LADCP shear velocity.

the trough. The fact that the top of the mooring does not reach the surface gives a comparatively small error since the surface water is close to freezing temperature.

In order to estimate the heat flux from the mooring data, an effective width of the inflow must be assumed. The trough has been transected twice at this location, in 2008 (Wåhlin et al. 2010) and 2010 (Fig. 2a). Both transects show a warm current spread out over about 100 km and isopycnals approximately parallel to the bottom. Effective widths for these transects can be estimated as the ratio between the geostrophic heat flux and the heat flux per unit width at the mooring, that is,

$$W = \frac{\int_{X_E}^{X_W} \int_{-D}^{-d} \overline{[T(z,t) - T_R]U_P} \, dz \, dx}{\int_{-D}^{-d} \overline{[T(z,t) - T_R]U_P} \, dz}. \qquad (2)$$

The ratio (2) was evaluated using geostrophic velocities and potential temperatures (interpolated to the midpoint between CTD stations) from the transects in 2008 and 2010. The effective widths thus obtained were 71 and 84 km in 2008 and 2010, respectively. Lacking other estimates, a constant effective width of 80 km was assumed, that is,

$$\mathrm{HF_{IN}} \approx \rho C_P W \int_{-D}^{-d} \overline{[T(z,t) - T_R]U_P} \, dz, \qquad (3)$$

where $W = 80$ km.

3. Results

Figures 2a–c show cross-trough sections of temperature, salinity, and velocity. At the eastern flank there is an inflow of warm water, where the sloping isotherms drive a geostrophic bottom current similar to the observed LADCP shear velocities. This agrees qualitatively with previous observations from the trough (Wåhlin et al. 2010, 2013; Arneborg et al. 2012). On the western flank the interface is tilted in the opposite direction, presumably driving a geostrophic outflow away from land. The westernmost stations in the sections are approximately 400 m deep, and hence the deepest geostrophic calculation point in the west is at 400 m, that is, above the outflow core (Fig. 2) and quite close to the reference level of 300 m. The geostrophic velocity between 300 and 400 m is negative, similar to LADCP velocities, although the main core is not visible in the geostrophic velocities due to the depth limit. From Fig. 2 the outflow was estimated to be about 40 km wide. Figure 2d shows a hydrographic section along the center of the trough in which the dense layer flows

southward along the bottom with a speed up to ~0.13 m s^{-1}.

Figure 3 shows progressive vector plots of velocities at different depths for the four moorings, color coded by temperature. There is a persistent inflow of warm deep water (temporal average: 0.8°C) on the eastern flank of DT. There is also an outflow of cooler and fresher water (temporal average: −0.4°C) along the bottom on the western side of the trough. This outflow is recorded in both M2 and M3, and it is likely the same current as observed in the westernmost parts of the transects (Figs. 2a–c). The flow direction near the bottom, where the warmest water is found, is parallel to the local bathymetry for both inflow and outflow. Also shown are 2-day low-pass-filtered velocities and temperatures. The seasonal variation of temperature is observed both in M1 and in M2, and shorter time scale variability is also significant in both moorings in particular for velocity (Figs. 3b–e). Long-term mooring time series are clearly necessary to make reliable budget calculations in this area.

The average inflow during 2011, 0.34 Sverdrups (Sv; 1 Sv ≡ 10^6 m^3 s^{-1}), is obtained through vertical integration of the average velocity at M1 and multiplication by the effective width of 80 km (section 2). The transport is similar to that estimated from a CTD/LADCP section in 2008 (Wåhlin et al. 2010). In 2010 the average transport was 0.21 Sv (Arneborg et al. 2012), so the annual variability is substantial.

Heat budgets

Figure 4 shows temperature–salinity diagrams for the moorings and historical data on the shelf. The black dashed line is the Gade line (Gade 1979; Jenkins 1999; Wåhlin et al. 2010). The bottom water at both M1 and M2 align on the Gade line, suggesting it consists of CDW modified by glacier meltwater. The cooler bottom water at M2 contains larger fractions of meltwater than the bottom water at M1. All the historical data have deep water that is warmer and saltier on the eastern flank than on the western flank.

Figure 5 shows the average velocity at the moorings for different temperature and salinity classes. There is an average inflow at M1 of water warmer than −1°C, with maximum velocity for $T \approx 0.75$°C and $S \approx 34.6$ psu. At M2, there is an average outflow of water with maximum velocity for $T \approx -0.5$°C and $S \approx 34.3$ psu. Figures 5c and 5d show the velocities in T–S diagrams. The velocities at M2 lines up on a colder part of the Gade line than at M1. It is also slightly colder than the Gade line suggesting that in addition to mixing with glacier meltwater, mixing with the cold surface water has also taken place on the shelf.

Provided the annual net volume and salt transports into the deep basin are zero we have
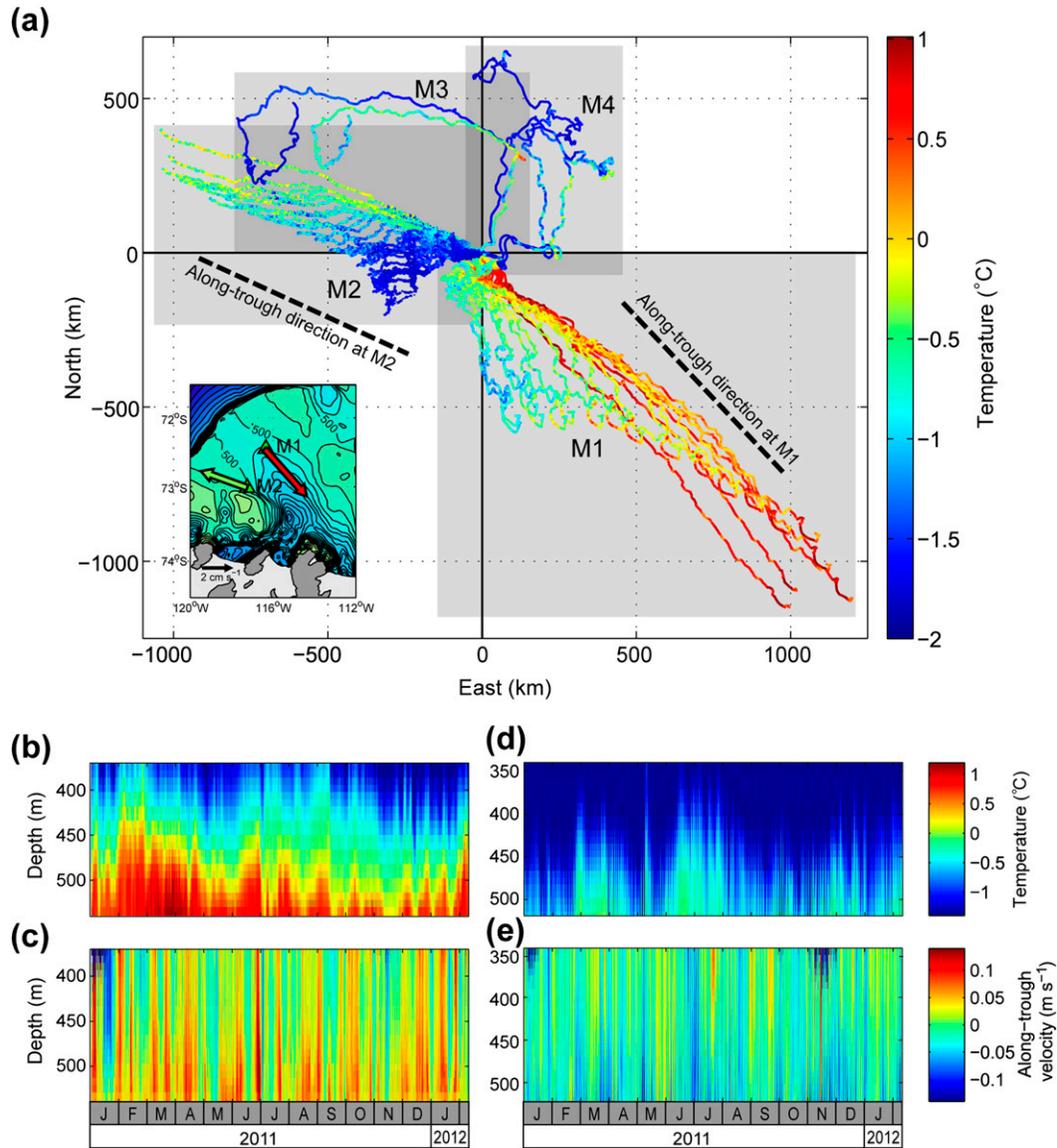
(a)

(b)

(c)

(d)

(e)

FIG. 3. (a) Progressive vector diagrams of velocities at the four moorings, color coded by temperature. Data from M1 and M2: the lines correspond to ADCP bins (every 8 m) and interpolated temperature. Data from M3: the two lines correspond to the velocity and temperature at 409- and 253-m depth. Data from M4: the two lines correspond to the velocity and temperature at 431- and 276-m depth. Start time is 1000 UTC 1 Jan 2011. The "along-trough direction" at M1 and M2 is indicated by black dashed lines. Each gray rectangle encompasses the data from the designated mooring. The inset shows vectors of time-averaged currents (color coded by temperature) near the bottom at M1 and M2. (bottom) The 2-day low-pass-filtered mooring data as a function of time and depth for M1 and M2. (b) Temperature and (c) along-trough velocity at M1; (d) temperature and (e) along-trough velocity at M2. Along-trough velocities are calculated by the direction given in (a), and negative velocities indicate northwestward flow.

$$Q_{\text{OUT}} = Q_{\text{IN}} + Q_F$$
$$\hat{S}_{\text{IN}} Q_{\text{IN}} = \hat{S}_{\text{OUT}} Q_{\text{OUT}}, \qquad (4)$$

where Q_{IN} and Q_{OUT} are the average volume flows into and out of the basin, Q_F is the average freshwater flux,

and $\hat{S}_{\text{IN}}$ and $\hat{S}_{\text{OUT}}$ are the velocity-weighted-average salinities of the inflow and outflow. Expression (4) can be assumed to hold if the measurement period is long compared to the overturning time of the deep water in the basin. An estimate of the overturning time, about 4 months, is obtained by dividing the basin volume
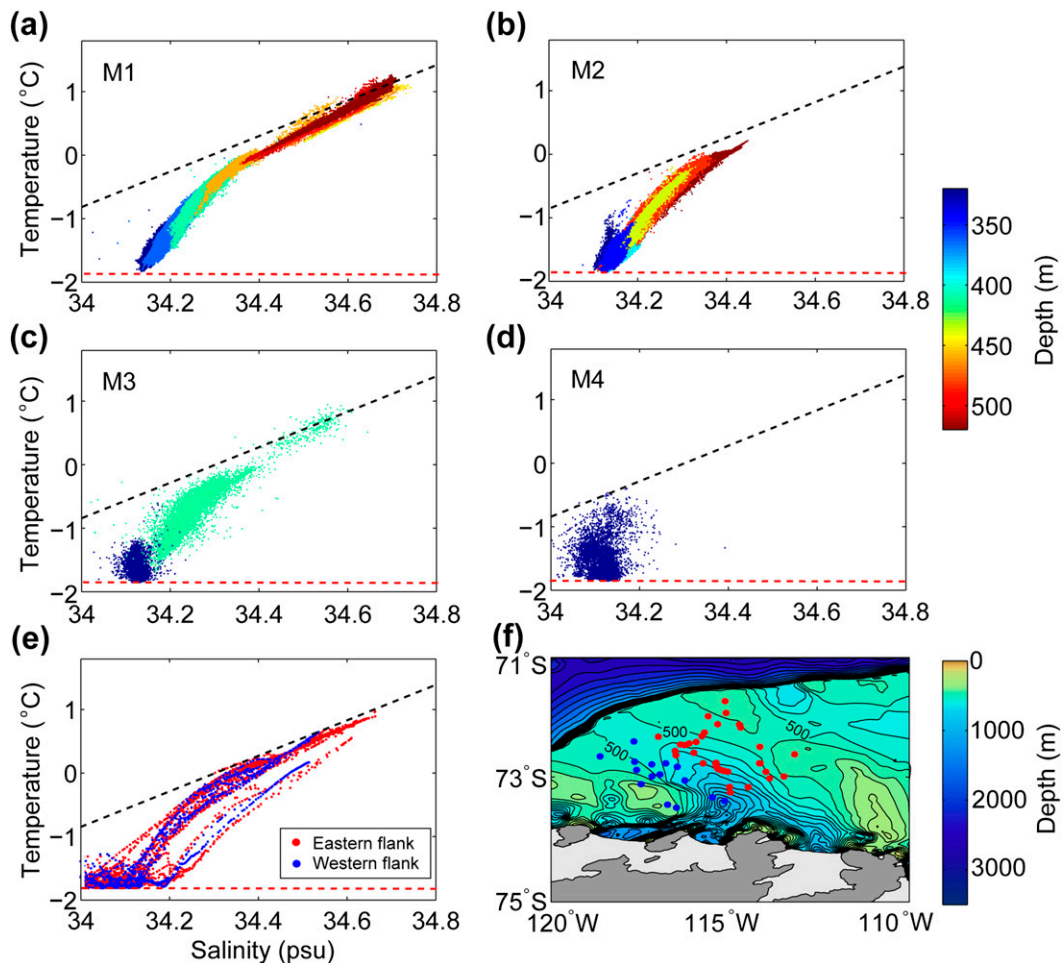
FIG. 4. Temperature–salinity diagrams in the moorings and CTD stations. (a)–(d) Daily averages of temperature and salinity at the moorings (color coded by depth). (e) Eastern (red) and western (blue) flanks of the DT, from historical data (i.e., from the *Oden* and *Araon* expeditions during 2008–12 and the *Palmer* in 1994, 2007, and 2009; Boyer et al. 2006). Black and red dashed lines represent the Gade line and freezing temperature, respectively. (f) Location of historical CTD stations.

$(3500 \, \text{km}^3)$ by the average inflow of 0.34 Sv. This is also close to the time it takes for the bottom water to travel 300 km, which is the circumference of the basin (Fig. 3a).

From (4), we can express Q_F as

$$Q_F = Q_{\text{IN}} \frac{\hat{S}_{\text{IN}} - \hat{S}_{\text{OUT}}}{\hat{S}_{\text{OUT}}}. \tag{5}$$

It is hence sufficient to know the inflow transport Q_{IN} and the two salinities $\hat{S}_{\text{IN}}$ and $\hat{S}_{\text{OUT}}$ in order to estimate the freshwater flux.

In Fig. 2 the outflow on the western flank was approximately 40 km wide. Vertical integration of the velocity at M2 and multiplication by 40 km gives an average outflow of 0.12 Sv, that is, only one-third of the inflow. The missing outflow can take place, for example,

in uncharted deep troughs farther west, in a coastal current, or in the surface layer. The theoretical maximum meltwater content that the outflow water can contain is given by the intersection between the Gade line and the freezing point ($T_M = -1.84°C$ and $S_M = 33.6 \, \text{psu}$; Fig. 5). The minimum meltwater content is likely given by the salinity $\hat{S}_2$ at M2, because all other possible outflow routes would contain lighter water, that is, larger meltwater fractions. An intermediate outflow salinity that is a weighted average of these is given by

$$\hat{S}_{\text{OUT}} = \frac{1}{3}\hat{S}_2 + \frac{2}{3}S_M, \tag{6}$$

where the fraction ⅓ comes from the ratio between inflow and outflow estimates, which in turn depend on the observed widths and velocities of the inflow and outflow.
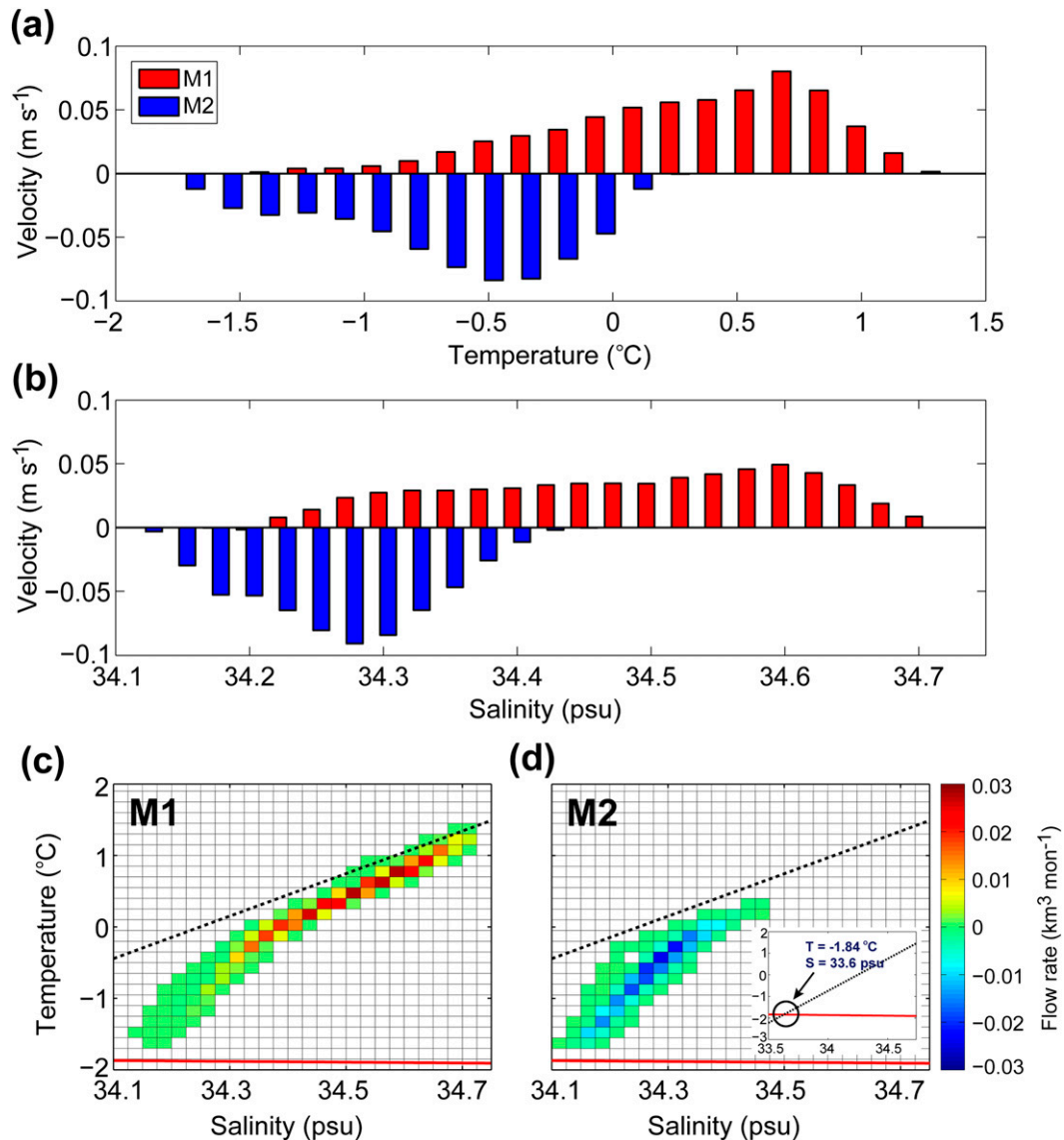
FIG. 5. Average flow rate per unit area as a function of (a) temperature (bars show 0.15°C bins) and (b) salinity (bars show 0.025 psu bins). Red bars show the warmer and saltier inflow at M1; blue bars show the colder and fresher outflow at M2. (c) Temperature–salinity diagram with colors indicating average flow rate per unit area for M1. (d) Temperature–salinity diagram with colors indicating average flow rate per unit area for M2. Dashed black line indicates the Gade line, and inset shows the intersection point between the Gade line and the freezing point.

Table 1 summarizes three budget calculations based on the three salinities. The lower bound ($\hat{S}_{\text{OUT}} = \hat{S}_2$) gives $Q_F = 2.6$ mSv, equivalent to 83 Gt yr^{-1} of glacial melt. This corresponds to 0.89 TW latent heat to ice melting. The upper bound ($\hat{S}_{\text{OUT}} = S_M$) gives $Q_F = 10.1$ mSv (316 Gt yr^{-1} of glacial melt), which corresponds to 3.36 TW latent heat. The intermediate salinity (6) gives $Q_F = 7.6$ mSv (237 Gt yr^{-1} of glacial melt), which corresponds to 2.53 TW latent heat. Using the temperature and velocity at M1 in (3) gives HF$_{\text{IN}} = 3.35$ TW. The

outflowing oceanic heat is obtained from an integral corresponding to (3) giving 1.6 TW for the lower bound, 0.53 TW for the weighted average, and 0 TW for the upper bound.

The difference between the inflow, the outflow, and the latent heat flux should be lost to the cold surface layer, giving an average heat loss of 17 W m^{-2} for the lower bound, 6 W m^{-2} for the weighted average, and -0.2 W m^{-2} for the upper bound. Using an average temperature stratification of 0.01 K m^{-1} (Fig. 3b), a vertical diffusivity κ_V of

TABLE 1. Calculations of upper, lower, and weighted-average budgets for heat and freshwater flux for the Dotson trough. The table shows inflow ($Q_{IN} = W_1 \int_{-D}^{-d} U_P^1 \, dz$, where $W_1 = 80$ km is the effective width of the inflow, and U_P^1 is the along-trough velocity at mooring M1), velocity-weighted-average salinity for the inflow [$\hat{S}_{IN} = \hat{S}_1 = (W_1 \int_{-D}^{-d} \overline{S_1 U_P^1} \, dz)/Q_1$, where S_1 is the salinity at mooring M1], and the outflow ($\hat{S}_{OUT}$); freshwater flux Q_F calculated according to (5); glacial melt (GM) corresponding to the freshwater flux Q_F, inflow heat flux HF_{IN} calculated according to (4); latent heat loss from glacial melt [$HF_L = LQ_F\rho$, where L (kJ kg^{-1}) is the latent heat of melting] and outflow heat flux (HF_{OUT}). Also shown is the amount of cooling needed in order to balance the heat budget (ie., $\Delta HF = HF_{IN} - HF_L - HF_{OUT}$) and the average heat flux per unit area required to balance the budget [i.e., $\Delta HF/A$, where $A = 50\,000$ km^2 is the approximate surface area of the central shelf (deeper than 200 m)]. The first column shows the upper estimate of the glacial melt (i.e., $\hat{S}_{OUT} = S_M$ and $HF_{OUT} = 0$). The last column shows the lower estimate of the glacial melt [i.e., $\hat{S}_{OUT} = \hat{S}_2 = (\int_{-D}^{-d} \overline{S_2 U_P^2} \, dz)/(\int_{-D}^{-d} \overline{U_P^2} \, dz)$, where S_2 is the salinity at mooring M2, U_P^2 is the along-trough velocity at mooring M2, and $HF_{OUT} = HF_2$ calculated according to (4) based on the mooring data at M2]. The center column shows a weighted average of the lower and upper estimates [i.e., $\hat{S}_{OUT} = (1/3)\hat{S}_2 + (2/3)S_M$ and $HF_{OUT} = (1/3)HF_2$].

	Upper estimate	Weighted average	Lower estimate
Q_{IN} (Sv)	0.339	0.339	0.339
$\hat{S}_{IN}$ (psu)	34.47	34.47	34.47
$\hat{S}_{OUT}$ (psu)	33.6	33.81	34.23
Q_F (mSv)	10.1	7.6	2.6
GM (Gt yr^{-1})	316	237	83
HF_{IN} (TW)	3.35	3.35	3.35
HF_L (TW)	3.36	2.53	0.89
HF_{OUT} (TW)	0	0.53	1.59
ΔHF (TW)	−0.01	0.29	0.87
$\Delta HF/A$ (W m^{-2})	−0.2	5.8	17.4

$\kappa_V = 4.2 \times 10^{-4}$ m^2 s^{-1} is required to balance the heat budget for the lower estimate, and $\kappa_V = 1.4 \times 10^{-4}$ m^2 s^{-1} for the weighted average. These values can be compared to those found on the central shelf in 2009 (Gerringa et al. 2012): $\kappa_V = 0.8 \times 10^{-5}$ m^2 s^{-1} for ice-covered water, $\kappa_V = 5.8 \times 10^{-5}$ m^2 s^{-1} in the polynya, and $\kappa_V = 9 \times 10^{-4} - 18 \times 10^{-4}$ m^2 s^{-1} in front of DIS and GIS. Bearing in mind that the continental shelf is ice covered most of the year, the weighted-average budget estimate appears more likely than the lower. It should be emphasized though that all measurements of κ_V as well as surface salinity are based on summertime data.

4. Discussion

The hydrographic data in this study show that CDW flowed southward along the eastern side of DT at the average flow rate of 0.34 Sv. A current transporting cooler and fresher versions of CDW northward on the western side of the trough was also found. The northward flow was seen in the hydrographic transects and found to be a persistent feature in two of the moorings. The observed width of the outflow at the time of the transects and the average velocity at the mooring indicate that only about one-third of the outflow exits as deep, warm water at M2. Alternative escape routes for the product water are westward in a coastal current, in the surface layer, below the GIS, or in the deep troughs farther west. Of these, a coastal current appears a quite likely alternative. The width of a coastal current would be approximately equal to the internal Rossby radius, that is, a few kilometers. Much denser station spacing than previously undertaken would hence be needed to resolve it. Jacobs et al. (2013) show the presence of low salinity water (33.7–33.8 psu) at 100-m depth by the coast near 135°W, indicating that a current carrying freshwater may have been present there in both 1994 and 2007.

The only study of a possible throughflow below the GIS (Jacobs et al. 2013) indicates a net eastward deep flow, depositing 0.2 Sv of water denser than $\sigma > 27.47$ into DT. Since the temporal variability is high (Fig. 3; Arneborg et al. 2012; Wåhlin et al. 2013) and the volume budget was based on snapshots (Jacobs et al. 2013), those findings are, however, uncertain. The present mooring observations indicate that, if anything, a westward deep flow below GIS is more likely than an eastward.

The obtained meltwater estimates are equivalent to 83–316 Gt yr^{-1} of ice with the intermediate value 237 Gt yr^{-1} corresponding to more likely values of turbulent diffusivity. They agree qualitatively with recent satellite-based measurements of the basal melt rates of the GIS of 145 Gt yr^{-1} and DIS of 45 Gt yr^{-1} (Rignot et al. 2013). The observed flow pathway for the deep water is sketched in Fig. 1. It is hypothesized that a deep circulation similar to the observed is at least intermittently prevailing also in the eastern part of the Amundsen Sea. Recent studies have shown hydrography with a northward deep geostrophic flow at the western flank (Nakayama et al. 2013) and generally warmer and saltier versions of the CDW in the east than in the west (Wåhlin et al. 2012; Assmann et al. 2013).

REFERENCES

Arneborg, L., A. K. Wåhlin, G. Björk, B. Liljebladh, and A. H. Orsi, 2012: Persistent inflow of warm water onto the central

Amundsen shelf. *Nat. Geosci.,* **5,** 876–880, doi:10.1038/ngeo1644.

Assmann, K. M., A. Jenkins, D. R. Shoosmith, D. Walker, S. Jacobs, and K. Nicholls, 2013: Variability of circumpolar deep water transport onto the Amundsen Sea continental shelf through a shelf break trough. *J. Geophys. Res. Oceans,* **118,** 6603–6620, doi:10.1002/2013JC008871.

Boyer, T. P., and Coauthors, 2006: *World Ocean Database 2005.* NOAA Atlas NESDIS 60, 190 pp.

Gade, H. G., 1979: Melting of ice in sea water: A primitive model with application to the Antarctic Ice Shelf and icebergs. *J. Phys. Oceanogr.,* **9,** 189–198, doi:10.1175/1520-0485(1979)009<0189:MOIISW>2.0.CO;2.

Gerringa, L. J. A., and Coauthors, 2012: Iron from melting glaciers fuels the phytoplankton blooms in Amundsen Sea (Southern Ocean): Iron biogeochemistry. *Deep-Sea Res. II,* **71–76,** 16–31, doi:10.1016/j.dsr2.2012.03.007.

Jacobs, S., A. Jenkins, C. F. Giulivi, and P. Dutrieux, 2011: Stronger ocean circulation and increased melting under Pine Island Glacier ice shelf. *Nat. Geosci.,* **4,** 519–523, doi:10.1038/ngeo1188.

——, C. Giulivi, P. Dutrieux, E. Rignot, F. Nitsche, and J. Mouginot, 2013: Getz ice shelf melting response to changes in ocean forcing. *J. Geophys. Res.,* **118,** 4152–4168, doi:10.1002/jgrc.20298.

Jenkins, A., 1999: The impact of melting ice on ocean waters. *J. Phys. Oceanogr.,* **29,** 2370–2381, doi:10.1175/1520-0485(1999)029<2370:TIOMIO>2.0.CO;2.

——, P. Dutrieux, S. S. Jacobs, S. D. McPhail, J. R. Perrett, A. T. Webb, and D. White, 2010: Observations beneath Pine Island Glacier in West Antarctica and implications for its retreat. *Nat. Geosci.,* **3,** 468–472, doi:10.1038/ngeo890.

Nakayama, Y., M. Schröder, and H. Hellmer, 2013: From circumpolar deep water to the glacial meltwater plume on the eastern Amundsen shelf. *Deep-Sea Res. I,* **77,** 50–62, doi:10.1016/j.dsr.2013.04.001.

Nitsche, F. O., S. S. Jacobs, R. D. Larter, and K. Gohl, 2007: Bathymetry of the Amundsen Sea continental shelf: Implications for geology, oceanography, and glaciology. *Geochem. Geophys. Geosyst.,* **8,** Q10009, doi:10.1029/2007GC001694.

Padman, L., H. A. Fricker, R. Coleman, S. Howard, and L. Erofeeva, 2002: A new tidal model for the Antarctic ice shelves and seas. *Ann. Glaciol.,* **34,** 247–254, doi:10.3189/172756402781817752.

Pritchard, H. D., R. J. Arthern, D. G. Vaughan, and L. A. Edwards, 2009: Extensive dynamic thinning on the margins of the Greenland and Antarctic Ice Sheets. *Nature,* **461,** 971–975, doi:10.1038/nature08471.

——, S. R. M. Ligtenberg, H. A. Fricker, D. G. Vaughan, M. R. van den Broeke, and L. Padman, 2012: Antarctic Ice-Sheet loss driven by basal melting of ice shelves. *Nature,* **484,** 502–505, doi:10.1038/nature10968.

Rignot, E., J. L. Bamber, M. R. van den Broeke, C. Davis, Y. Li, W. J. van de Berg, and E. van Meijgaard, 2008: Recent Antarctic ice mass loss from radar interferometry and regional climate modeling. *Nat. Geosci.,* **1,** 106–110, doi:10.1038/ngeo102.

——, S. Jacobs, J. Mouginot, and B. Scheuchl, 2013: Ice-shelf melting around Antarctica. *Science,* **341,** 266–270, doi:10.1126/science.1235798.

Thurnherr, A. M., 2010: A practical assessment of the errors associated with full-depth LADCP profiles obtained using Teledyne RDI Workhorse acoustic Doppler current profilers. *J. Atmos. Oceanic Technol.,* **27,** 1215–1227, doi:10.1175/2010JTECHO708.1.

Visbeck, M., 2002: Deep velocity profiling using lowered acoustic Doppler current profiler: Bottom track and inverse solutions. *J. Atmos. Oceanic Technol.,* **19,** 794–807, doi:10.1175/1520-0426(2002)019<0794:DVPULA>2.0.CO;2.

Wåhlin, A. K., X. Yuan, G. Björk, and C. Nohr, 2010: Inflow of warm circumpolar deep water in the central Amundsen shelf. *J. Phys. Oceanogr.,* **40,** 1427–1434, doi:10.1175/2010JPO4431.1.

——, R. D. Muench, L. Arneborg, G. Björk, H. K. Ha, S. H. Lee, and H. Alsén, 2012: Some implications of Ekman Layer dynamics for cross-shelf exchange in the Amundsen Sea. *J. Phys. Oceanogr.,* **42,** 1461–1474, doi:10.1175/JPO-D-11-041.1.

——, and Coauthors, 2013: Variability of warm deep water in a submarine trough on the Amundsen Sea shelf. *J. Phys. Oceanogr.,* **43,** 2054–2070, doi:10.1175/JPO-D-12-0157.1.